Investigation of hydrogen peroxide reduction reaction on graphene and nitrogen doped graphene nanoflakes in neutral solution

Seyed Javad Amirfakhri*, Dustin Binny, Jean-Luc Meunier, Dimitrios Berk

Department of Chemical Engineering, McGill University, 3610 University Street, Montreal, Quebec H3A 0C5, Canada

HIGHLIGHTS

- Nitrogen doped graphene with high nitrogen content (32 at% N) is synthesized.
- H_2O_2 reduction is studied on both graphene and nitrogen doped graphene nanoflakes.
- The reaction rate of H_2O_2 reduction on graphene increases noticeably by N-doping.
- H_2O_2 reduction occurs by the same mechanism on both graphene and N-doped graphene.
- H_2O_2 decomposition occurs as a side reaction on both graphene and N-doped graphene.

GRAPHICAL ABSTRACT
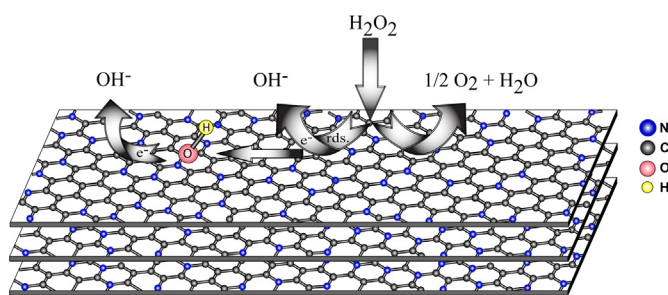
ABSTRACT

H_2O_2 reduction reaction (HPRR) is studied on both graphene (GNF) and nitrogen doped graphene nanoflakes in 0.1 M Na_2SO_4 solution by rotating disk electrode. The XPS results indicate that N-doped graphene nanoflakes with high nitrogen content, 32 at%N (N-GNF32), are synthesised successfully by an inductively-coupled thermal plasma (ICP) reactor. Pyridinic, pyrrolic and graphitic N species contribute up to 67% of the total nitrogen. Kinetic parameters such as Tafel slope and stoichiometric number suggest that HPRR occurs by the same mechanism on both GNF and N-GNF32. Although nitrogen does not change the mechanism of HPRR, the results indicate that the reaction rate of H_2O_2 reduction is enhanced on N-GNF32. The exchange current density of H_2O_2 reduction based on the active surface area of N-GNF32 is $(8.3 \pm 0.3) \times 10^{-9}$ A cm^{-2}, which is 6 times higher than the value determined for GNF. The apparent number of electrons involved in the process suggests that H_2O_2 decomposition competes with H_2O_2 reduction on both catalysts. Evaluation of the apparent heterogeneous reaction rate constant and the Tafel slope indicate that simultaneous reduction of O_2 and H_2O_2 is negligible on the N-GNF32. On the other hand, the reduction of O_2 and H_2O_2 occurs simultaneously on the GNF surface.

© 2014 Elsevier B.V. All rights reserved.

1. Introduction

Nitrogen doped carbon nano-materials have been studied widely to replace the conventional metallic catalysts in fuel cells [1,2]. N-doping is a method to increase the catalytic activity of carbon nano-materials toward the oxygen reduction reaction (ORR); however, the phenomena responsible for the enhancement

* Corresponding author. Tel.: +1 514 398 4494; fax: +1 514 398 6678.
   E-mail addresses: seyed.amirfakhri@mail.mcgill.ca, jamirfakhri@gmail.com (S. J. Amirfakhri).

of the catalytic activity for nitrogen-doped carbon nano-materials are largely unknown and still controversial [1,3,4].

Nitrogen doped graphene is one of the new catalyst structures that has received a great of attention in recent years particularly in the context of the oxygen reduction reaction (ORR) [5,6]. Graphene is a two dimensional form of carbon which shows special characteristics such as high crystallinity helping to maintain stability, high specific surface area and electrical conductivity. Different types of nitrogen species in the graphene lattice present different catalytic performance toward ORR. For instance Lai et al. [7] showed that while the graphitic N species noticeably increase the limiting current density, the pyridinic N shifts the onset potential towards more positive values. Moreover, pyridinic N species might change the ORR mechanism from the series (Eq. (1)) to the direct dominated pathway (Eq. (2)).

$$O_2 + 2e^- + 2H^+ \rightarrow H_2O_2 \tag{1}$$

$$O_2 + 4e^- + 4H^+ \rightarrow 2H_2O \tag{2}$$
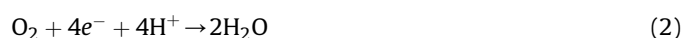
Although ORR has been studied extensively, few results have been reported on the reduction of H_2O_2 using N-doped graphene as a catalyst. Hydrogen peroxide has been investigated as an alternative oxidant to oxygen in fuel cells for several reasons [8—10]. First, H_2O_2 has a much higher solubility than oxygen in water; it is thus easily accessible in the liquid phase at higher concentrations than oxygen. The use of an aqueous oxidant which is more soluble in water than dissolved oxygen is a possible solution for an increase of the power density of fuel cells. Second, the hydrogen peroxide reduction reaction (HPRR) shows a lower activation barrier in comparison to the oxygen reduction reaction (ORR). The HPRR is an electrochemical reaction involving two electrons being transferred, while a four-electron transfer reaction occurs in the ORR. Finally, H_2O_2 is a suitable candidate for space and underwater applications where air is not readily accessible to supply oxygen for fuel cells.

The most important disadvantage of using H_2O_2, however, is the H_2O_2 decomposition. H_2O_2 can be reduced following Eq. (3) and/or decompose to oxygen on the electrode surface through Eq. (4). H_2O_2 decomposition causes the partial loss of the reactant, decreases the power density of the fuel cell and can also block the reactant flow inside small microfluidic fuel cells [11,12].

$$H_2O_2 + 2e^- + 2H^+ \rightarrow 2H_2O \tag{3}$$

$$2H_2O_2 \rightarrow O_2 + 2H_2O \tag{4}$$

Among the noble metal catalysts, gold exhibits high catalytic activity towards H_2O_2 reduction while partially inhibiting H_2O_2 decomposition [13,14]. Non-metal as well as non-noble metal catalysts of various types have also been studied for HPRR [15—18]. Recently, Shao et al. [19] studied HPRR on N-doped graphene qualitatively in a quiescent solution. The results of cyclic voltammetry and chronoamperometry indicated that N-doped graphene produces much higher current densities in comparison to pure graphene. However, no information has been reported on the kinetic parameters such as the exchange current density or the mechanism of HPRR occurring on N-doped graphene structures.

Very recently the H_2O_2 reduction mechanism has been studied by Wu et al. [20] on both graphene and N-doped graphene using density functional theory (DFT) calculations. Their results indicate that the H_2O_2 adsorption on both graphene and N-doped graphene occurs through a weak physical bond (physisorption). Moreover, two paths are suggested for the H_2O_2 reduction on both graphene and N-doped graphene. In the first path the adsorbed H_2O_2, thereafter called $(H_2O_2)_{ads}$, receives an electron to produce adsorbed OH,

$(OH)_{ads}$. Then $(OH)_{ads}$ receives another electron to produce water. In the second path, the $(H_2O_2)_{ads}$ first breaks to two $(OH)_{ads}$ and then $(OH)_{ads}$ obtains one electron to produce water. In the latter path the electrochemical step is repeated twice to complete the process. According to the calculation of the Gibbs free energy of different reactions involved in these paths, the first path is suggested by Wu et al. for the H_2O_2 reduction on both graphene and N-doped graphene. It is also suggested that the pyridinic N atoms should exhibit the best performance for the H_2O_2 reduction.

In this research, the catalytic activity of nitrogen doped graphene nano-flakes (N-GNF) with 32% nitrogen content (thereafter labelled N-GNF32) and pure graphene nano-flakes (GNF) are studied experimentally for HPRR in a neutral electrolyte (0.1 M Na_2SO_4) by the rotating disk electrode (RDE) technique. Pyridinic, pyrrolic and graphitic N species constitute 67% of the total nitrogen of N-GNF32. The objectives of the current work include (1) the determination of the kinetic parameters for HPRR on both graphene and N-doped graphene, (2) an evaluation of H_2O_2 decomposition according to the determined kinetic parameters, (3) a comparison of the reaction rates on the catalysts, and (4) the suggestion of a mechanism for the H_2O_2 reduction on both graphene and N-doped graphene according to the kinetic parameters determined experimentally. Finally, the produced current density on GNF and N-GNF32 are compared with gold.

2. Experimental

2.1. Materials and measurements

The synthesis methods of GNF and N-GNF32 have been reported in detail elsewhere [21]. In summary, an inductively-coupled thermal plasma (ICP) reactor uses the dissociation of methane precursor to produce pure graphene nanoflakes through controlled homogeneous nucleation of the carbon vapour at high temperatures. N-doped graphene with different nitrogen content can be generated *in situ* using a nitrogen plasma as a post treatment on the GNF powders within the reactor. Transmission electron microscopy (TEM), and X-ray photoelectron spectroscopy (XPS) were used to characterize the morphology and evaluate the elemental composition of the samples. The Brunauer—Emmett—Teller (BET) method from nitrogen gas adsorption—desorption isotherms at 77 K was used to determine the specific surface area of the powders. The details of the working electrode preparation and the electrochemical tests are presented in the Supporting information, section 1 and 2. The H_2O_2 concentration in the control experiment was measured using the Idiometric method [22].

The active surface area of the electrodes was determined by voltammetry method [23]. In this method, the double layer charging current (i_{dl}) is measured at different scan rates. A linear relation is expected between the double layer charging current and scan rate sr = dE/dt, its slope being used to determine the apparent total double layer capacitance of the electrode (C_A) according to Eq. (5) where Q is the charge transferred.

$$C_A = \frac{dQ}{dE} = \frac{i_{dl}}{\left(\frac{dE}{dt}\right)} = \frac{i_{dl}}{sr} \tag{5}$$

The active surface area is then obtained by dividing the apparent total double layer capacitance to the double layer capacitance available from the literature. The specific active surface area is determined by dividing the active surface area with the catalyst mass. The exchange current densities are normalized to the active surface areas in order to determine the intrinsic effect of the catalyst structure on HPRR.

Table 1
XPS results of the samples(at%): GNF and N-GNF32.

Sample	N	C	O
GNF	0	98.1 ± 0.3	1.8 ± 0.4
N-GNF32	32.4 ± 0.2	63.7 ± 0.5	3.3 ± 0.5

3. Results and discussion

HPRR was investigated on GNF, N-GNF32 and gold in a neutral solution (0.1 M Na_2SO_4) by RDE. Before the tests, the stability of H_2O_2 in 0.1 M Na_2SO_4 solution was evaluated to ensure that H_2O_2 decomposition, if any, only occurs on the electrode and not in the bulk solution. For this test, a concentration of 0.1 M of H_2O_2 in a 0.1 M Na_2SO_4 solution was used as a control experiment, the H_2O_2 concentration being measured in 30 min time intervals. The results of this control experiment indicated that H_2O_2 concentration started to decrease slightly after 1 h. After 2 h, more than 97% of H_2O_2 was still available in the solution indicating that H_2O_2 is reasonably stable for sufficiently long periods of time in this solution to complete the electrochemical tests.

3.1. Catalyst characterization

The nitrogen, carbon and oxygen ratios on the series of GNF and N-GNF32 samples used in the present experiments are given in Table 1 following XPS analysis, confirming the large amount of nitrogen present in the N-GNF32 [21]. The results demonstrated that atomic nitrogen levels over 30 at%N on the carbon support

were achieved. The distribution of the nitrogen was 24%, 28%, and 15% in pyridinic, pyrrolic and graphitic sites, respectively. No metal impurities were detected in the synthesised samples.

The TEM images in Fig. 1 show the structure of both GNF and N-GNF-32. These are made of an average of 10 graphene layers (number of layers varying between 5 and 20) and have planar dimensions typically in the range between 50 and 100 nm. The large nitrogen content is believed to occur mainly on the surrounding edges of the stacked graphene planes structure.

The BET specific surface area of the samples was measured as 345 and 130 m^2 g^{-1} for GNF and N-GNF32, respectively. These values are much lower than the specific surface area of an individual graphene sheet (2600 m^2 g^{-1}) suggesting the presence of multilayer graphene and N-doped graphene sheets [24]. This result is consistent with the observation from TEM. Moreover, the BET specific surface area of the N-GNF32 is unexpectedly 3 times lower than the GNF. Generally, the specific surface area of graphene is expected to increase after N-doping because of inducing more disorder in the graphene lattice. Agglomeration of the graphene nanoflakes in the post-treatment process to produce N-GNF32 might be a reason for the low BET results determined in our work although the TEM observations do not seem to show any morphological changes. A decrease of the specific surface area of graphene after nitrogen functionalization has also been reported by Sheng et al. [25].

3.1.1. Determination of specific active surface area

Fig. 2(a) shows the polarization data of a GNF electrode in 0.5 M H_2SO_4 solution. Cyclic voltammograms in the potential range from
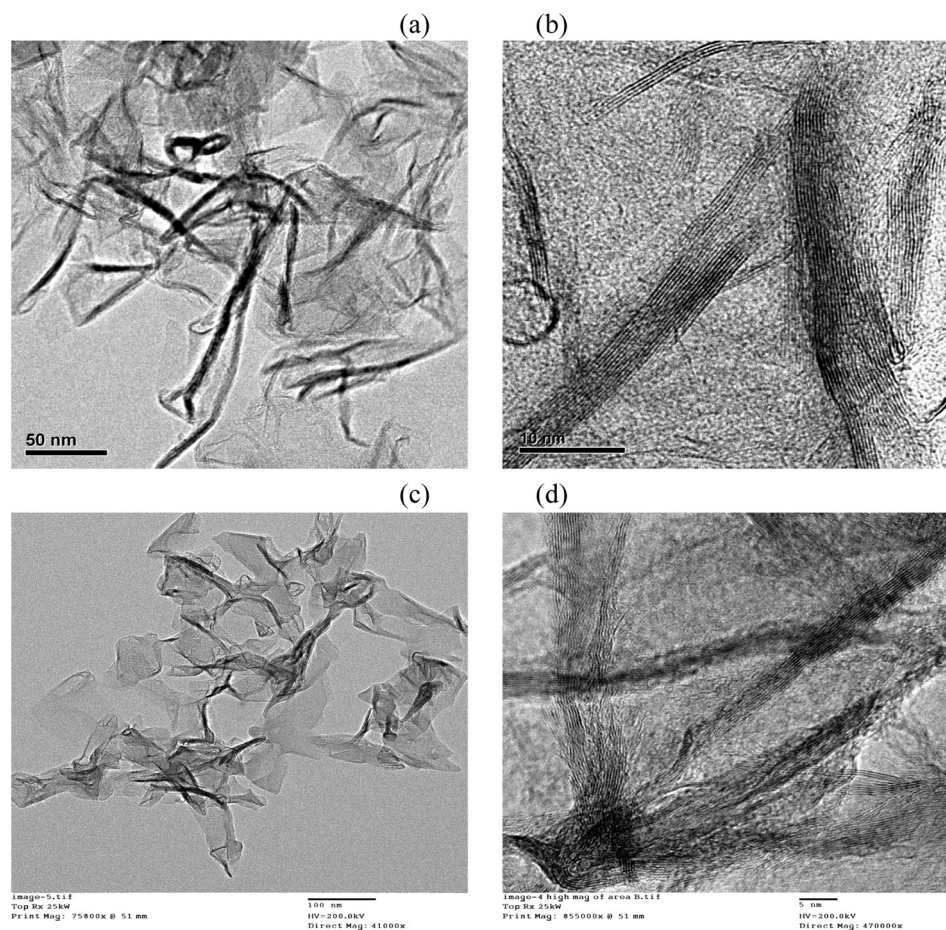

Fig. 1. TEM images of the catalysts: GNF with low (a) and high magnifications (b), and N-GNF32 with low (c) and high magnifications (d).
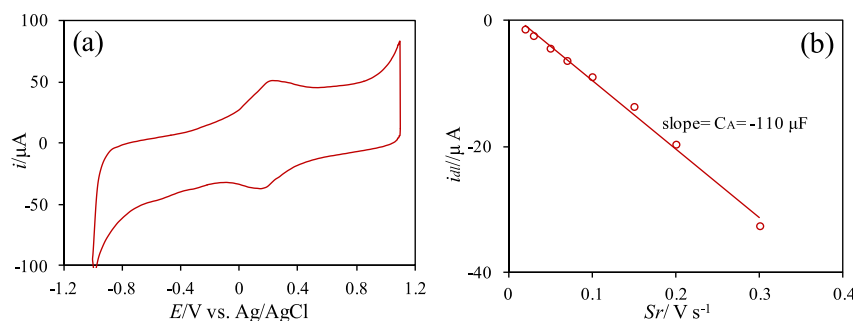
Fig. 2. (a) Polarization data of a GNF electrode (catalyst loading = 50 µg cm^{-2}) in 0.5 M H$_2$SO$_4$ solution in the absence of H$_2$O$_2$ (scan rate = 100 mV s^{-1}). (b) Determination of the apparent total double layer capacitance by plotting double layer charging current (E = 0.75 V vs. Ag/AgCl) versus scan rate.

1 to 0.5 V vs. Ag/AgCl with different scan rates show almost a flat current plateau suggesting the absence of faradic reactions in this area of potentials. Thus the potential range between 1 and 0.5 V vs. Ag/AgCl was assumed to be the double layer region and the current in the middle of this region was employed to determine the apparent total double layer capacitance. Fig. 2(b) presents the measurement of the total double layer capacitance of a GNF electrode at E = 0.75 V vs. Ag/AgCl.

The double layer capacitance of graphene sheets has been reported between 2 and 21 µF cm^{-2} [26,27]. By assuming first a double layer capacitance of 7 µF cm^{-2}, the specific active surface area of GNF was 165 ± 10 m^2 g^{-1}. The active surface area determined by voltammetry is less than 50% of the total surface area determined by the BET method suggesting that most of the catalyst surface area is not accessible to the electrolyte. If one assumes a higher double layer capacitance reaching 30 µF cm^{-2}, the specific active surface area of N-GNF32 is found to be 36.7 ± 3 m^2 g^{-1} (data not shown here).

3.2. HPRR on the N-GNF32 electrode

Fig. 3(a) presents the steady state hydrodynamic voltammograms of the N-GNF32 electrode in 1 mM H$_2$O$_2$ + 0.1 M Na$_2$SO$_4$ at different rotation rates. The Koutecky−Levich equation, Eq. (6), can be used to determine the apparent number of electrons n involved in the HPRR process, and the apparent heterogeneous reaction rate constant k of H$_2$O$_2$ reduction by plotting j^{-1} vs. $\omega^{-1/2}$ at different electrode potentials:

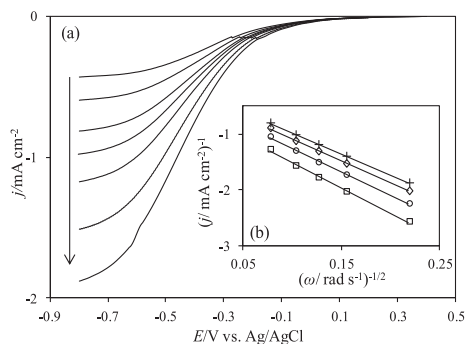$$\frac{1}{j} = \frac{-1}{nFkc} - \frac{1}{0.62nFD^{\frac{2}{3}}v^{-\frac{1}{6}}c\omega^{\frac{1}{2}}} \qquad (6)$$

where D is the diffusion coefficient of H$_2$O$_2$ (9 × 10^{-6} cm^2 s^{-1}) [22,28], v is the kinematic viscosity of the solution (0.01 cm^2 s^{-1}), c is the bulk concentration of H$_2$O$_2$ (in this case, c = 1 × 10^{-6} mol cm^{-3}), and ω is the rotation rate of the electrode (rad s^{-1}). Fig. 3(b) shows the Koutecky−Levich plots for the mixed control (mass and kinetic control) region of voltammograms. Straight and reasonably parallel lines infer that the reaction is indeed first order with respect to the H$_2$O$_2$ concentration.

The reaction order m was also determined as 1.16 ± 0.07 by plotting log(j) vs. log(1 − j/j_d), confirming that the reaction is first order with respect to the H$_2$O$_2$ concentration (see Fig. S1 in the Supporting information).

The apparent number of electrons involved in HPRR was determined from the slope of the Koutecky−Levich plots (Fig. 3(b)) at different electrode potentials. Fig. 4 shows that n is a function of the electrode potential and increases while the electrode potential shifts toward more negative potentials. The apparent number of electrons less than 2 suggests that the decomposition of H$_2$O$_2$ competes with the reduction of H$_2$O$_2$ at low overpotentials. While the H$_2$O$_2$ decomposition rate is independent of the electrode potential, the H$_2$O$_2$ reduction rate is a strong function of overpotential and increases at high overpotentials. Hence, at sufficiently high electrode potentials (E < −0.45 V) the H$_2$O$_2$ reduction overcomes the H$_2$O$_2$ decomposition resulting in n approaching the expected value of n = 2 in Eq. (3).

The values of k were calculated by using Eq. (6) and the intercepts of the lines in Fig. 3(b) at different potentials. The apparent heterogeneous electron-transfer rate constants strongly depended on the electrode potential (Table 2), suggesting that the rate determining step is an electron transfer reaction and not a chemical reaction [13,29,30].
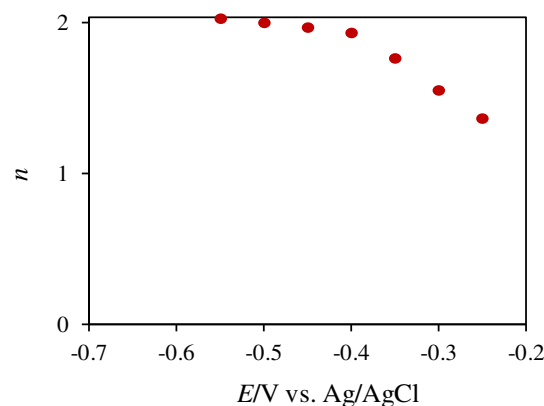

Fig. 3. (a) Steady state hydrodynamic voltammograms of the N-GNF32 electrode in 1 mM H$_2$O$_2$ + 0.1 M Na$_2$SO$_4$ at different rotation rates: 100, 200, 400, 600, 900, 1600, and 2500 rpm in arrow direction (scan rate = 10 mV s^{-1}, catalyst loading = 250 µg cm^{-2}). (b) Koutecky−Levich plots for reduction of 1 mM H$_2$O$_2$ at different potentials: −0.45 V (□), −0.5 V (○), −0.55 (◇), and −0.6 V (+). Data are obtained from Fig. 3(a).

Fig. 4. Apparent number of electrons for the reduction of 1 mM H$_2$O$_2$ on the N-GNF32 electrode at different potentials. Data are obtained from the slope of Koutecky−Levich plots (Fig. 3(b)).

Table 2
The apparent heterogeneous electron-transfer rate constants (k) of HPRR on the N-GNF32 electrode at different electrode potentials.

E (V)	−0.3	−0.35	−0.4	−0.45	−0.5	−0.55	−0.6
k (cm s^{-1})	0.0023	0.0038	0.0056	0.0081	0.013	0.022	0.029

3.2.1. Tafel slope analysis

Tafel equation, Eq. (7), [31,32] was used to construct Tafel plots at different rotation rates.

$$\eta = \frac{2.3RT}{\alpha_c n_\alpha F}(\log j - \log j_0) \tag{7}$$

where η is the overpotential (V), α_c is the cathodic transfer coefficient, n_α is the total number of electron(s) involved in the rate determining step and all previous step(s), and j_0 is the exchange current density based on the geometric surface area of the electrode (A cm^{-2}). Eq. (7) can be used to determine the α_c and j_0 from the slope and the intercept of the line between η and log(j).

Fig. 5(a) shows that for high enough overpotentials (higher than 35 mV) two Tafel slopes are observed: at overpotential more positive than −90 mV, the Tafel slope was −127 mV, while it was almost doubled at overpotentials more negative than −90 mV. Doubled Tafel slope phenomena at high overpotentials can occur in porous electrodes and have been explained in detail [33–35]. Tafel slope analysis was repeated for different rotation rates and a Tafel slope of 125 ± 2 mV was obtained suggesting that the first electron transfer is the rate determining step ($n_\alpha = 1$). Using the Tafel slope at different rotation rates, $n_\alpha = 1$, and Eq. (7), the cathodic transfer coefficient α_c can be evaluated as 0.47 ± 0.01. The exchange current density based on the geometric surface area was then found to be $(7.7 \pm 0.3) \times 10^{-7}$ A cm^{-2}. Using the active specific surface area of N-GNF32, a value of $(8.3 \pm 0.3) \times 10^{-9}$ A cm^{-2} was determined as the exchange current density based on the active surface area of the electrode (j_{0A}).

The mass transfer corrected form of the Tafel equation was also used to determine the Tafel slope in the mixed control region of hydrodynamic voltammograms [31,36,37]. Fig. 5(b) shows that the Tafel slope at different rotation rates between 100 and 2500 rpm is constant (268 ± 2 mV) and independent of the rotation rate suggesting that the simultaneous reduction of H$_2$O$_2$ and O$_2$ is negligible [13,38].

3.2.2. Stoichiometric number determination

The stoichiometric number (ε) is defined as the number of times the rate determining step is occurring in order to complete one cycle of the overall reaction. The stoichiometric number is determined from the following equation [39];
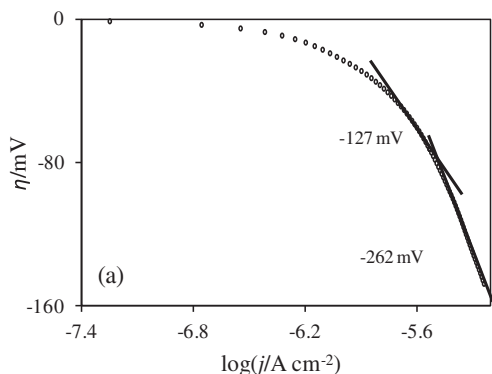

Fig. 6. Determination of the slope of j vs. η at very low overpotentials, $(\partial j/\partial \eta)_{\eta \to 0}$. Data are obtained from Fig. 3(a) for $\omega = 100$ rpm.

$$\varepsilon = \frac{nFj_0}{RT\left(\frac{\partial j}{\partial \eta}\right)_{\eta \to 0}} \tag{8}$$

where $(\partial j/\partial \eta)_{\eta \to 0}$ is the slope of j vs. η when η approaches zero. Fig. 6 shows the relation between j and η at very low overpotentials for a rotation rate of 100 rpm. The stoichiometric number was determined to be 1.14 by using the slope of Fig. 6 and Eq. (8) while $j_0 = 8.03 \times 10^{-7}$ A cm^{-2}.

The stoichiometric number was determined for different rotation rates from 70 to 400 rpm and a mean value of $\varepsilon = 1.17 \pm 0.15$ was obtained. This value is close to 1 suggesting that the rate determining step occurs one time in order to complete one cycle of HPRR on this catalyst. The stoichiometric number was also determined as $\varepsilon = 1$ by the graphical method of Allen and Hickling (see Fig. S2 in the Supporting information) indicating consistency in the data.

3.2.3. HPRR mechanism on N-GNF32

A complete mechanistic analysis of HPRR is complex and its details are beyond the scope of the present work. In this section, the kinetic parameters determined in the previous sections are used to propose a mechanism for HPRR.

According to the kinetic parameters determined in this work and different mechanisms proposed for HPRR in the literature [13,40–42], the following mechanism is suggested for HPRR on N-GNF32 (NG in these reactions representing the nitrogen doped graphene):

$$NG + H_2O_2 \leftrightarrow NG \cdot H_2O_2 \tag{9}$$

Fig. 5. (a) Tafel plots for HPRR on the N-GNF32 electrode in 1 mM H$_2$O$_2$ + 0.1 M Na$_2$SO$_4$ ($\omega = 100$ rpm). Data are obtained from the kinetic control region of Fig. 3(a). (b) Mass transfer corrected form of Tafel plots at different rotation rates. j_d is determined from the Levich equation by using $n = 2$. The current densities are obtained from mixed control region of Fig. 3(a).
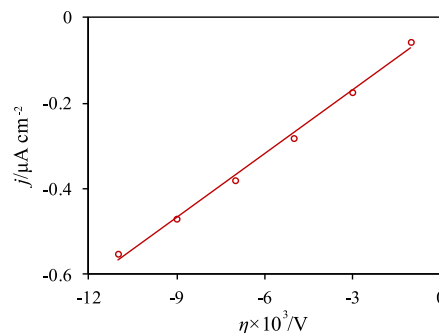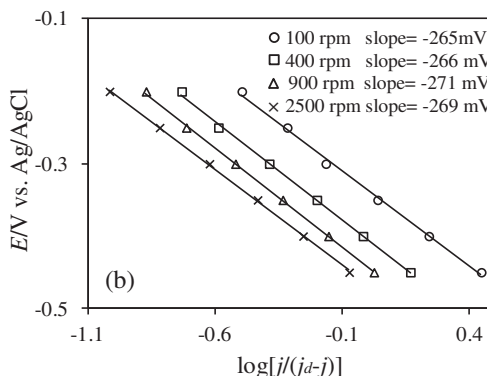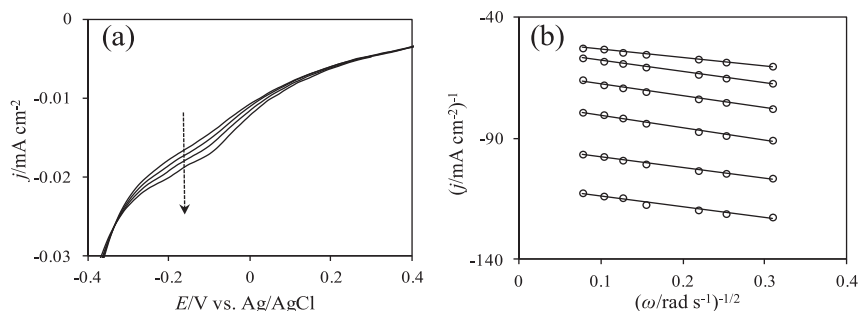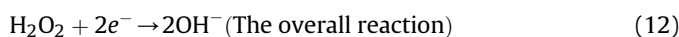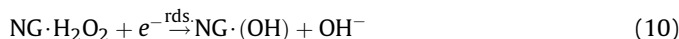
Fig. 7. (a) Hydrodynamic voltammograms of reduction of 1 mM H_2O_2 in 0.1 M Na_2SO_4 solution on the GNF electrode at different rotation rates; 100, 200, 400, and 1600 rpm in the arrow direction (scan rate = 10 mV s^{-1}, catalyst loading = 250 µg cm^{-2}). (b) Koutecky—Levich plots at different electrode potentials; 0.1, 0.05, 0, −0.05, −0.1, and −0.15 V vs. Ag/AgCl from the bottom to the top.

$$NG \cdot H_2O_2 + e^- \xrightarrow{\text{rds.}} NG \cdot (OH) + OH^- \qquad (10)$$

$$NG \cdot (OH) + e^- \leftrightarrow NG + OH^- \qquad (11)$$

$$H_2O_2 + 2e^- \rightarrow 2OH^- \text{ (The overall reaction)} \qquad (12)$$

This mechanism satisfies all the evidence obtained in our work: 1) the first electron transfer as the rate determining step, 2) a first order reaction with respect to H_2O_2 concentration, 3) a stoichiometric number equal to 1, and 4) negligible reduction of O_2. Moreover, this mechanism is consistent with the mechanism suggested by Wu et al. [20] for H_2O_2 reduction on N-doped graphene explained in the introduction.

At low overpotentials both H_2O_2 reduction and decomposition occur on the electrode surface with comparable reaction rates. Therefore, reaction (4) competes with reaction (10). These results support the equation and methodology that have recently been developed in our group for analysis of HPRR [43].

3.3. HPRR on the GNF electrode

In this section the H_2O_2 reduction on the GNF electrode is studied and the kinetic parameters are determined. In order to evaluate the catalytic effect of nitrogen on the graphene structure, the kinetic parameters of HPRR on N-GNF32 and GNF are then compared.

Fig. 7(a) presents the RDE results of H_2O_2 reduction on the GNF electrode in 0.1 M Na_2SO_4 solution. The current density shows a weak dependence to the rotation rate suggesting that H_2O_2 reaction rate is very slow on the GNF. The current density becomes

independent of rotation rate at $E < -0.3$ V. These results suggest that H_2O_2 is relatively stable on the GNF.

Fig. 7(b) presents the Koutecky—Levich plots of the H_2O_2 reduction on the GNF electrode. The apparent number of electrons involved in the HPRR was 0.37 ± 0.07. This value is noticeably smaller than the value determined for N-GNF32 suggesting that H_2O_2 decomposition is not negligible in the studied potential window.

The apparent heterogeneous reaction rate constant of the H_2O_2 reduction was determined from the intercepts of the lines in Fig. 7(b). Generally, the reaction rate constant of an electrochemical reaction is a strong function of overpotential, and a linear relation is expected between η (or E) and $\log(k)$ with a slope equal to the Tafel slope [32].

Fig. 8 presents the relation between E and $\log(k)$ for reduction of 1 mM H_2O_2 on the GNF electrode. The large Tafel slope (−685 mV) observed in this figure can be a sign for a chemical electrochemical reaction mechanism (CE reaction mechanism) when the chemical reaction is the rate determining step [44]. This result suggests that the H_2O_2 decomposition to O_2 (Eq. (4)), followed by the O_2 reduction (Eqs. (1) and (2)), is not negligible on GNF in the mixed control region of voltammograms. The CE reaction mechanism can also infer to the slow H_2O_2 adsorption followed by the H_2O_2 reduction.

The Tafel slope in the mixed control region of hydrodynamic voltammograms was determined by the mass transfer corrected form of Tafel equation. Fig. 9 indicates the Tafel slope is a function of rotation rate, confirming that both H_2O_2 and O_2 reduction occur simultaneously in this potential region.

The Tafel slope and cathodic transfer coefficient in the kinetic control region, evaluated using Eq. (7), were 118 ± 2 mV and 0.5 ± 0.01, respectively. These are very close to the values
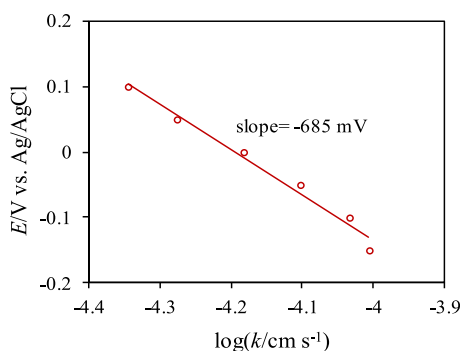

Fig. 8. The relation between E and $\log(k)$ for the reduction of H_2O_2 on GNF. Large Tafel slope (−685 mV) is a sign for an electrochemical reaction with a slow preceding chemical reaction.
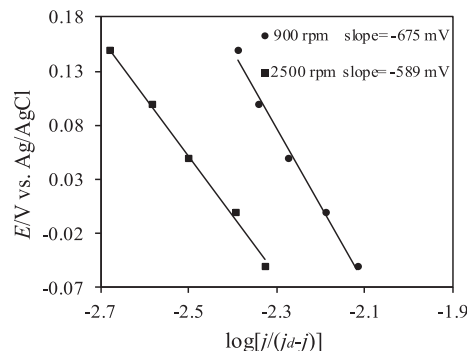

Fig. 9. The mass transfer corrected form of the Tafel slope for the H_2O_2 reduction on GNF. Data are obtained from Fig. 7(a). j_d was determined from the Levich equation by using $n = 0.45$.

Table 3
Kinetic parameters for H_2O_2 reduction on GNF and N-GNF32 in 0.1 M Na_2SO_4 solution.

	n	J_{0A} (A cm^{-2})	Tafel slope (low overpotentials)	α_c	ε	H_2O_2 decomposition	Simultaneous reduction of O_2 and H_2O_2
GNF	0.37 ± 0.07	$(1.52 \pm 0.03) \times 10^{-9}$	118 ± 2	0.5 ± 0.01	1	Yes	Yes
N-GNF32	1.8 ± 0.25	$(8.3 \pm 0.3) \times 10^{-9}$	125 ± 2	0.47 ± 0.01	1	Yes	Negligible

determined as 125 ± 2 mV and 0.47 ± 0.01 for the H_2O_2 reduction on N-GNF32. The stoichiometric number was also determined as 1.12 ± 0.04. These results highly suggest that the H_2O_2 reduction takes place by the same mechanism on both GNF and N-GNF.

The exchange current density based on the active surface area of GNF, j_{0A}, was $(1.52 \pm 0.03) \times 10^{-9}$ A cm^{-2} at low overpotentials. This value is almost 6 times smaller than the determined value of j_{0A} for N-GNF32, $(8.3 \pm 0.3) \times 10^{-9}$ A cm^{-2}. The exchange current densities based on the active surface areas indicate that higher catalytic activity of N-GNF32 is an intrinsic effect of nitrogen atoms on the graphene lattice, irrespective of the surface area. This result is consistent with the result reported by Wang et al. [3] for O_2 reduction on graphite nitride. They showed that the higher catalytic activity of graphite nitride in comparison with graphite and graphite oxide is created by nitrogen atoms which facilitate the electron transfer from carbon to O_2. Moreover, the effect of geometric factors such as surface area was reported to be negligible.

A summary of the determined kinetic parameters for the reduction of H_2O_2 on GNF and N-GNF32 is presented in Table 3.

3.4. Comparison between HPRR on GNF, N-GNF32 and gold

Fig. 10 presents the current densities produced by the reduction of 1 mM H_2O_2 in 0.1 M Na_2SO_4 solution on three different electrodes: GNF, N-GNF32, and gold at 400 rpm. Comparison between current densities produced on GNF and N-GNF32 indicates that nitrogen doping increases the H_2O_2 reduction rate which is consistent with the determined exchange current densities. However the produced current density by N-GNF32 is still lower than gold electrode. Employing N-doped graphene with different nitrogen composition (higher atomic percentage of pyridinic and/or graphitic N species) and using other dopants such as iron and boron may be a solution to increase the produce current density in order to compete with gold.

4. Conclusion

Although both catalysts, GNF and N-GNF32, employed in this work present high BET surface areas, determination of the active surface areas show that more than 50% of the areas are not accessible for the electrochemical reactions.

The results indicate that N-doping facilitates the H_2O_2 reduction on graphene while it does not change the mechanism of the process. Determination of the Tafel slope, transfer coefficient and stoichiometric number at low overpotentials indicate that H_2O_2 is reduced by the same mechanism on both GNF and N-GNF32.

The H_2O_2 reduction and decomposition occur at similar reaction rates on N-GNF32 at $E > -0.45$ V. By shifting the potential toward more negative potentials than -0.45 V, the HPRR becomes dominant and the number of electron approaches 2. Tafel slope analysis and determination of the apparent heterogeneous reaction rate constant in the mixed control region of voltammograms reveal that the simultaneous reduction of O_2 and H_2O_2 is negligible on N-GNF32.

Steady state hydrodynamic voltammograms demonstrate that the HPRR occurs at limited potentials ($E > -0.3$ V) on GNF. At potentials more negative than -0.3 V, the RDE voltammograms lose their dependency on the rotation rate suggesting that H_2O_2 is stable in this potential region.

Although N-doping facilitates the reduction reaction of H_2O_2, the current density produced on N-GNF32 is still smaller than that on a gold catalyst. Further studies are required to possibly increase the current density of N-doped graphene catalyst structures, and understand the effect of different N types involved in the graphene lattice or from other dopants.

Acknowledgements

Appendix A. Supplementary data

Supplementary data related to this article can be found at http://dx.doi.org/10.1016/j.jpowsour.2014.01.114.

References

[1] K. Gong, F. Du, Z. Xia, M. Durstock, L. Dai, Science 323 (2009) 760—764.
[2] T. Sharifi, G. Hu, X. Jia, T. Wågberg, ACS Nano 6 (2012) 8904—8912.
[3] P. Wang, Z. Wang, L. Jia, Z. Xiao, Phys. Chem. Chem. Phys. 11 (2009) 2730—2740.
[4] P. Wu, Y. Qian, P. Du, H. Zhang, C. Cai, J. Mater. Chem. 22 (2012) 6402—6412.
[5] D. Geng, Y. Chen, Y. Chen, Y. Li, R. Li, X. Sun, S. Ye, S. Knights, Energy Environ. Sci. 4 (2011) 760—764.
[6] L. Qu, Y. Liu, J.-B. Baek, L. Dai, ACS Nano 4 (2010) 1321—1326.
[7] L. Lai, J.R. Potts, D. Zhan, L. Wang, C.K. Poh, C. Tang, H. Gong, Z. Shen, J. Lin, R.S. Ruoff, Energy Environ. Sci. 5 (2012) 7936—7942.
[8] Y. Wang, Z. Guo, Y. Xia, Adv. Energy Mater. 3 (2013) 713—717.
[9] E. Kjeang, A.G. Brolo, D.A. Harrington, N. Djilali, D. Sinton, J. Electrochem. Soc. 154 (2007) B1220—B1226.
[10] A.E. Sanli, A. Aytaç, Int. J. Hydrogen Energy 36 (2011) 869—875.
[11] E. Kjeang, N. Djilali, D. Sinton, J. Power Sources 186 (2009) 353—369.
[12] J.-C. Shyu, C.-L. Huang, J. Power Sources 196 (2011) 3233—3238.
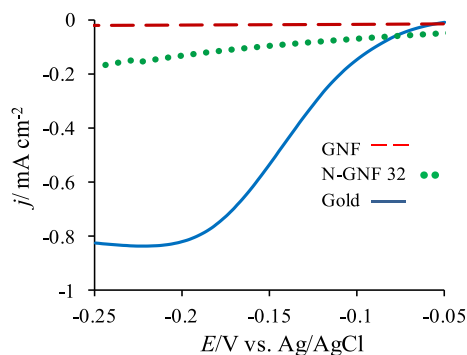[13] R.R. Adić, N.M. Marković, V.B. Vešović, J. Electroanal. Chem. Interfacial Electrochem. 165 (1984) 105—120.

Fig. 10. Hydrodynamic voltammograms for the reduction of 1 mM H_2O_2 in 0.1 M Na_2SO_4 solution on three different electrodes with the same geometric surface area: GNF (dashed line), N-GNF32 (dotted line), and gold (solid line) ($\omega = 400$ rpm).

[14] L. Gu, N. Luo, G.H. Miley, J. Power Sources 173 (2007) 77—85.
[15] S.A. Mousavi Shaegh, N.-T. Nguyen, S.M. Mousavi Ehteshami, S.H. Chan, Energy Environ. Sci. 5 (2012) 8225—8228.
[16] G. Wang, Y. Bao, Y. Tian, J. Xia, D. Cao, J. Power Sources 195 (2010) 6463—6467.
[17] R.C. Peña, J.C. Gamboa, M. Bertotti, T.R. Paixão, Int. J. Electrochem. Sci. 6 (2011) 394—403.
[18] X.-M. Miao, R. Yuan, Y.-Q. Chai, Y.-T. Shi, Y.-Y. Yuan, J. Electroanal. Chem. 612 (2008) 157—163.
[19] Y. Shao, S. Zhang, M.H. Engelhard, G. Li, G. Shao, Y. Wang, J. Liu, I.A. Aksay, Y. Lin, J. Mater. Chem. 20 (2010) 7491—7496.
[20] P. Wu, P. Du, H. Zhang, C. Cai, Phys. Chem. Chem. Phys. 15 (2013) 6920—6928.
[21] D.M. Binny, J.-L. Meunier, D. Berk, in: 12th IEEE Conference on Nanotechnology (IEEE-NANO), Birmingham, 2012.
[22] W.C. Schumb, C.N. Satterfield, R.L. Wentworth, Hydrogen Peroxide, Reinhold Pub. Corp., New York, 1955.
[23] S. Trasatti, O.A. Petrii, Pure Appl. Chem. 63 (1991) 711—734.
[24] G. Srinivas, Y. Zhu, R. Piner, N. Skipper, M. Ellerby, R. Ruoff, Carbon 48 (2010) 630—635.
[25] Z.-H. Sheng, L. Shao, J.-J. Chen, W.-J. Bao, F.-B. Wang, X.-H. Xia, ACS Nano 5 (2011) 4350—4358.
[26] J. Xia, F. Chen, J. Li, N. Tao, Nat. Nanotechnol. 4 (2009) 505—509.
[27] E. Uesugi, H. Goto, R. Eguchi, A. Fujiwara, Y. Kubozono, Sci. Rep. 3 (2013) 1—5.
[28] J.S. Jirkovsky, M. Halasa, D.J. Schiffrin, Phys. Chem. Chem. Phys. 12 (2010) 8042—8053.
[29] R.W. Zurilla, R.K. Sen, E. Yeager, J. Electrochem. Soc. 125 (1978) 1103—1109.
[30] A. Damjanovic, M.A. Genshaw, J.O.M. Bockris, J. Electrochem. Soc. 114 (1967) 1107—1112.
[31] A.J. Bard, L.R. Faulkner, Electrochemical Methods: Fundamentals and Applications, second ed., John Wiley & Sons, Inc., 2001.
[32] R. Greef, R. Peat, L.M. Peter, D. Pletcher, J. Robinson, Instrumental Methods in Electrochemistry, Ellis Horwood Limited, 1985.
[33] J.N. Soderberg, A.C. Co, A.H.C. Sirk, V.I. Birss, J. Phys. Chem. B 110 (2006) 10401—10410.
[34] B.V. Tilak, S. Venkatesh, S.K. Rangarajan, J. Electrochem. Soc. 136 (1989) 1977—1982.
[35] J.O.M. Bockris, S. Srinivasan, Fuel Cells: Their Electrochemistry, McGraw-Hill, 1969.
[36] K.L. Hsueh, D.T. Chin, S. Srinivasan, J. Electroanal. Chem. Interfacial Electrochem. 153 (1983) 79—95.
[37] K.I. Vasu, M. Noel, Cyclic Voltammetry and the Frontiers of Electrochemistry, Aspect, London, 1990.
[38] N.M. Marković, R.R. Adić, V.B. Vešović, J. Electroanal. Chem. Interfacial Electrochem. 165 (1984) 121—133.
[39] R. Parsons, Trans. Faraday Soc. 47 (1951) 1332—1344.
[40] A. Damjanovic, M.A. Genshaw, J.O.M. Bockris, J. Electroanal. Chem. Interfacial Electrochem. 15 (1967) 173—180.
[41] F.W. Campbell, S.R. Belding, R. Baron, L. Xiao, R.G. Compton, J. Phys. Chem. C 113 (2009) 9053—9062.
[42] J. Wilshire, D.T. Sawyer, Acc. Chem. Res. 12 (1979) 105—110.
[43] S.J. Amirfakhri, J.-L. Meunier, D. Berk, Electrochim. Acta 114 (2013) 551—559.
[44] K.L. Stewart, A.A. Gewirth, Langmuir 23 (2007) 9911—9918.